Title

Aeroacoustic Predictions of Free-Wake, Vortex Particle Method, and Computational Fluid Dynamics for a Coaxial Rotor System

Authors

Sharma, Kalki
Brentner, Kenneth S
Jia, Zhongqi
et al.

Publication Date

2020-01-20

Aeroacoustic Predictions of the Free-Wake Model, Vortex Particle Method, and Computational Fluid Dynamics for a Coaxial Rotor System

Kalki Sharma Ph.D. Candidate
Kenneth S. Brentner Professor
Penn State University
University Park, PA, USA

Zhongqi Jia Ph.D. Candidate
Seongkyu Lee Assistant Professor
University of California, Davis
Davis, CA, USA

Phuriwat Anusonti-Inthra
Aerospace Engineer
U.S. Army Combat Capabilities Development Command, Army Research Laboratory
Aberdeen Proving Ground, MD, USA

ABSTRACT

In this paper the aeroacoustic results using the Free-Wake Model (FWM), Vortex Particle Method (VPM), and Computational Fluid Dynamics (CFD) are compared with one another. The FWM and VPM is performed using the software Rotorcraft Comprehensive Analysis System (RCAS), and CFD analysis is performed using the software Helios. Analysis is performed on a lift-offset coaxial rotor system operating at 150 knots in forward flight and 0° shaft tilt. First, the blade loads are compared and then the acoustics using the noise prediction software PSU-WOPWOP. The major difference between the analysis methods is the manner in which they capture aerodynamic interactions. And the differences in the interactions result in differences in the acoustic results. The primary interactions are the blade vortex interactions (BVI), and the blade crossover interactions (BCI). The BVI events occur when a rotor operates in the wake of its own rotor or another rotor, and the BCI events occur when the blades of the upper and lower rotors cross one another. The BVI events are captured by all three methods, but there are variations in location and intensity between the three methods. On the other hand, the VPM and CFD capture the BCI events, but the VPM is unable to capture the BCI events on the retreating side of the upper rotor. These differences in the prediction of the interactions results in variations in directivity as well as intensity of the noise results. Upon analysis of the aeroacoustic results it is concluded that the inability of the FWM and VPM to capture some of the primary interactions capture by CFD can lead to major discrepancies between the acoustic results of the three methods.

INTRODUCTION

A coaxial helicopter is a rotorcraft configuration which relies on two coaxial, contra-rotating rotors for its primary flight capabilities. Many modern coaxial configurations also rely on additional vehicle components to augment the lift and/or thrust of the rotors – these vehicles are referred to as compound rotorcraft. Over the years, companies have researched and developed experimental compound configurations to overcome the limitations inherent in conventional helicopter designs. Recently, there has been renewed interest by the Department of Defense in the development of rotorcraft for the modern era. In 2009, the Secretary of Defense established the U.S. Future Vertical Lift (FVL) initiative (Ref. 2) with the goal to replace all the U.S. Department of Defense helicopters with next-generation rotorcraft in an effort to upgrade the performance and technological capabilities of the current rotorcraft fleet. One configuration that shows promise is the compound coaxial rotorcraft.

The compound coaxial is able to overcome limitations of the conventional helicopter by using the Advancing Blade Concept (ABC) rotor design (Ref. 1). The ABC rotor design allows each rotor of the coaxial configuration to carry a non-zero roll moment as long as the other rotor carries a roll moment of opposite direction and equal magnitude. When the rotor's roll moment is non-dimensionalized by the rotor's thrust and radius it is referred to as the lift-offset. The mathematical expression of lift-offset (L.O.) for a coaxial rotor is the following:

$$L.O. = \frac{\Delta M_x}{T_{total} R} \tag{1}$$

where ΔM_x is the differential roll moment between the two rotors, T_{total} is the combined thrust of the two rotors, and R is the rotor radius of a single rotor (assuming each rotor's radius is equal). The benefit of not constraining a rotor to operate at zero lift-offset is that the rotor blades are then able to operate at more optimal blade section angles of attack on the advancing side, avoid stall on the retreating side, and achieve higher forward flight speeds. In contrast, thrust production of conventional helicopters is limited because of retreating blade stall. As the rotor achieves a higher forward flight speed it is required to produce more thrust, and eventually the retreating side can no longer generate enough lift (due to retreating blade stall) to counteract the roll moment of the advancing side of the rotor. But without the constraint of each rotor having a

Presented at the Vertical Flight Society's Transformative Vertical Flight 2020 Forum at San Jose, California, Jan. 21-23. 2020.

zero roll moment the ABC coaxial rotor design can continue to have higher lift on the advancing side of the rotor as forward speed and rotor thrust are increased.

Along with the benefits of a coaxial configuration, there are also drawbacks due to the proximity of the upper and lower rotors to each other, and operation at high speed flight. These conditions result in interference between the two rotors along with interference of the individual rotors and their own wakes. The aerodynamic interference yields impulsive loading events such as blade-vortex interactions (BVI), and blade crossover interactions (BCI), which results in impulsive pressure loading peaks, and therefore, impulsive noise.

Previous studies which have used theoretical modeling to predict the noise of the coaxial rotor system have focused on the variation of certain parameters to obtain overall trends. In 2005 and 2006, Boyd et al. (Ref. 4) and Wachspress (Ref. 5), respectively, published papers analyzing the noise from a coaxial rotor system. Boyd and Wachspress both noted that the coaxial rotor system on average is louder than a conventional single rotor of equivalent solidity.

One of the major studies into the noise produced by a coaxial rotorcraft utilizing lift offset was conducted at the University of Glasgow (Ref. 6) in 2009. Kim et al. used the Vorticity Transport Model developed by Brown (Ref. 7) to analyze coaxial rotor systems of varying flapwise stiffness. The paper concluded that the major source of noise was the advancing side of the lower rotor due to the interaction between the upper rotor's wake and the lower rotor's advancing side blades. And that the noise could be reduced by increasing the lift offset, especially at the higher speed case.

Walsh et al. (Ref. 8) in 2016 published an investigation into higher-speed cases of the coaxial rotor system using prescribed wake analysis. The paper noted that rotor blade phasing could potentially be used to result in noise sources adding constructively or destructively, a phenomena unique to multirotor configurations. The paper also explored the acoustic benefits of operating the rotor system at lower rotation rates, and noted significant reductions in noise levels. Also in 2016, Barbely et al. (Ref. 9) published a paper exploring the interactions between the upper and lower rotor blades at the point of crossover. Barbely et al. noted a fluctuation in pressure that is a potentially important noise source, which at that time had not been explored for its acoustic impact.

In 2018 Herrmann et al. (Ref. 10) performed a multidisciplinary trim analysis of the coaxial rotor system using a free wake model and analyzed the influence of shaft tilt on the rotor noise. Herrmann noted that at 0° shaft tilt the noise is the greatest and at +5° shaft tilt the noise appears to be the lowest. Jia et al. (Ref. 12) conducted research into higher speed cases at 0° shaft tilt using CFD analysis, and varied the lift offset and rotor separation distance. Jia noted loading fluctuations appear when the lower rotor and upper rotor blades cross one another, and the noise due to BVI events reduces as the separation distance increases at certain flight speeds.

The research efforts cited in this section all aid in the understanding of the aeroacoustic environment of the coaxial rotor system, but the predictive capabilities of different analysis models on aeroacoustics has yet to be addressed. Research has been done into the aerodynamic predictive capabilities of varying levels of physics-based models for the coaxial rotor system by Jacobellis et al. (Ref. 13) and Klimchenko et al. (Ref. 11). But analysis has not been performed in the acoustic predictive capabilities. In this paper three aerodynamic modeling approaches - free-wake model (FWM), vortex particle method (VPM), and computational fluid dynamics (CFD) - are used to compute the blade loads. The accuracy of the physical model is critical to accurate prediction of the rotor system noise, but not all the flow features have the same acoustic significance. The focus of this paper is to perform aerodynamic and acoustic analysis of a lift-offset coaxial rotor system using mid- to high-fidelity analysis tools and analyze the most acoustically significant aspects of the aerodynamic models.

ANALYSIS MODELS

This section describes the approach used to perform the analysis of the coaxial rotor configuration. Modeling of the rotor geometry, blade dynamics, trim method, aerodynamic modeling, and acoustic prediction are all summarized in the following subsections.

Rotor & Trim Model

The rotor system analyzed in this paper is based on the Sikorsky XH-59A (Ref. 1). The primary rotor specifications are provided in Table 1. The rotor blades are modeled based on publicly available airfoils that match with the thickness distribution of the actual airfoils of the XH-59A. NACA-0026 is used at positions less than 42% span; NACA-63216 is used between 42% and 68% span; NACA-23012 is used at positions greater than 68% span. The elastic properties of the rotor blades are provided in Ruddell's report (Ref. 3) on the XH-59A altitude expansion and operational tests.

Table 1: XH-59A Rotor Characteristics.

Characteristic	English	Metric
Radius	18 ft	5.486 m
Number of Rotors	2	
Blades per Rotors	3	
Root Cut-Out	20%	
Blade Precone	3°	
Rotor Axial Separation	2.5 ft	0.76 m
Tip Speed	650 ft/s	198 m/s

The structure and connections of the rotor model are specified and analyzed in the software Rotorcraft Comprehensive Analysis System (RCAS) (Ref. 15). The model of the XH-59 rotor system used in this paper is based on the work of Jacobellis et al. (Ref. 16). The RCAS software is used to solve for the blade motion, loading, and deformation.

The rotor model is set up in RCAS such that the blades can be controlled through the feathering motion, but are rigidly attached in the lead-lag and flap directions. Elastic deformation is modeled for all three rotation motions. The trim methodology is specified in Table 2. The subscripts $_u$ and $_l$ refer to the upper and lower rotors, respectively. The term ΔM_x is the differential roll moment, and the trim target is user specified in order to achieve a specific lift offset value. The trim targets of M_x, M_y, and $\sum M_z$ are trimmed to zero, and F_z is trimmed to the vehicle's weight, which is approximately 11,900 lbs. The force in the x-direction is also trimmed by summing the rotor thrust, fuselage drag, rotor drag, and auxiliary propulsion thrust to zero. The fuselage drag coefficient used in the RCAS model is estimated based on the experiment conducted by Felker (Ref. 18) in the 40- by 80-foot wind tunnel at NASA Ames. It should be noted that a physical fuselage is excluded in the CFD model.

Table 2: Trim settings of rotor system.

Trim Variable	Equation	Trim Target
Collective	$\theta_o = \frac{\theta_u+\theta_l}{2}$	F_z
Lateral Cyclic	$\theta_c = \frac{\theta_{cu}+\theta_{cl}}{2}$	M_x
Longitudinal Cyclic	$\theta_s = \frac{\theta_{su}+\theta_{sl}}{2}$	M_y
Diff. Coll.	$\Delta\theta_o = \frac{\theta_u-\theta_l}{2}$	$\sum M_z$
Diff. Lat Cyclic	$\Delta\theta_c = \frac{\theta_{cu}-\theta_{cl}}{2}$	ΔM_x

Aerodynamic Modeling

The aerodynamic analysis is coupled with the computational structural dynamic (CSD) model in an iterative process such that the blade loads are computed along with the resulting blade deformations. The free-wake model and vortex particle method aerodynamic analysis are performed in RCAS and the CFD analysis is performed by Helios (Ref. 17). And RCAS performs the structural analysis for all three aerodynamic analysis methods. In this section the details of the aerodynamic models are outlined.

Free-Wake Model The free-wake model allows for mid-fidelity analysis of the rotor's flowfield by accounting for the influence of a rotor's wake. The analysis was performed using RCAS `v18.03.c6a`. The wake is modeled as discretized vortex filaments shed near the tip of the blade. The vortex filaments are free to deform to influences of the rotor's inflow, other filaments, and the filaments own influence acting on itself. But the wake is generated based on semi-empirical modeling, so assumptions are made about the wake's strength, trajectory, and vortex-blade interactions (e.g. core modeling). The tip vortex is shed every 3° azimuth and the wake extends 4 rotor revolutions.

By default, RCAS does not account for any interference effects from one rotor to another when performing aerodynamic analysis using FWM. So the user is required to specify the interference models for the rotors. The interference models account for the influence of the wake of one rotor on the other rotor's wake trajectory and rotor inflow via the Biot-Savart Law. For the case of the coaxial rotor configuration, the influence of the upper rotor's wake is experienced by the lower rotor and its wake, and vice-versa for the lower rotor's influence on the upper rotor.

The near wake age and the roll-up wake are set to 30°, such that there is no roll-up wake region and only a near and far wake. This is because an interaction should occur when the blades of the upper and lower rotors cross one another, but non-physical, impulsive loading events begin to occur for a coaxial configuration at the location of crossover. One way to avoid this issue is to set the set the near wake and roll-up wake age as equivalent.

Vortex Particle Method Another aerodynamic model run using RCAS `v19.10` is the viscous vortex particle method (VVPM) (Ref. 19). The VVPM RCAS model was used to account for complex aerodynamic interference between the upper and lower rotors. Examples of these interactions include inflow and blade cross-over interferences. These interferences may be difficult to capture using lower fidelity aerodynamic models (linear inflow or dynamic inflow models). However, the linear inflow model is used to calculate the initial trim parameters and blade deformations. The rotors are trimmed for specific thrust level and lift offset values. After the initial trim variables and blade deformations were calculated, the VVPM inflow model was activated and continued until the converged blade deformation, blade loading, VVPM induced velocity, and trim parameters were obtained. A brief description of the VVPM implementation is given here (see full details in (Ref. 19)). The VVPM solves the vorticity transport equation to determine the location and strength vectors of each vortex particle in the flow field. The location of each particle is calculated by integrating total induced velocity from all of the vortex particles. The induced velocity from each of the particle is obtained from modified Biot-Savart law to account for the viscous vortex core velocity distribution and to avoid numerical singularity at the center of the vortex. The strength of each particle is adjusted due to viscosity effect (vorticity redistribution method) and vortex stretching term. The vorticity source for the VVPM is the vortex particles (both trail and shed vorticity) released from the rotor blades at every time step. In the study, a total of 20-30 vortex particles are released along the span at each time step or one degree azimuth.

Computational Fluid Dynamics High-fidelity CFD/CSD loose coupling simulations are performed using the advanced rotorcraft simulation and comprehensive analysis software Helios (Ref. 20), which is being developed under the U.S. Department of Defense (DoD) Computational Research and Engineering Acquisition Tools and Environments - Air Vehi-

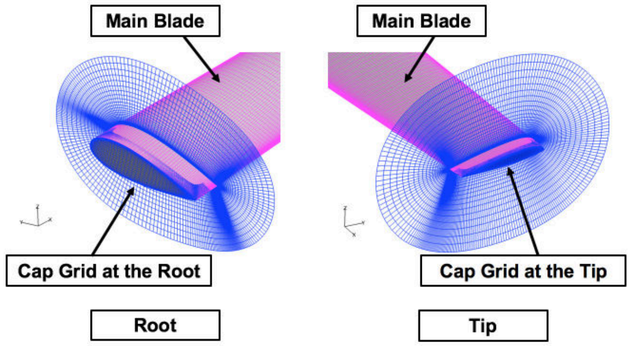

(a) The near-body grids.

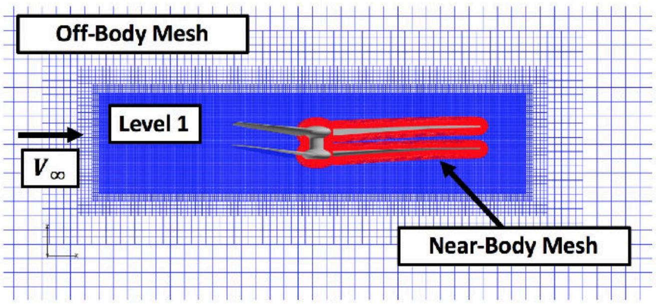

(b) The off-body grids.

Fig. 1: The CFD meshes.

cles (CREATE^{TM}-AV) program. The CFD/CSD loose coupling approach implemented in this research is the same as the approach of Potsdam et al. (Ref. 21). The CFD airloads are coupled to the CSD solver in an iterative manner starting from the second iteration until the convergence of blade airloads and trim solutions. The frequency of the CFD/CSD loose coupling is set to every 180 degrees azimuth (half rotor revolution) after the first rotor revolution.

The CFD simulations are conducted based on a dual-paradigm approach. The near-body structured overset grids are solved using the compressible finite-difference solver OVERFLOW (Ref. 22) while the off-body adaptive Cartesian grids are solved using SAMCart (Ref. 23) with adaptive mesh refinement capabilities. Figure 1 shows a zoomed-in views of near-body and off-body grids. Each main blade mesh is composed of 267 grid points in the chordwise direction, 189 grid points in the spanwise direction, and 65 grid points in the normal direction with leading and trailing edge spacings equal to 0.05% C_{tip} and 0.02% C_{tip} respectively, where C_{tip} is the tip chord length. A wall spacing of 5.0 $\times$ 10^{-4}% C_{tip} based on a dimensionless wall distance $y^+ = 1.0$ and an end spacing of 10% C_{tip} are used for near-body grids. The distance of each near-body grid in the normal direction is approximately 1.0 C_{tip}. Each rotor blade has approximately 5 million grid points.

The adaptive off-body mesh is constructed based on eight levels of AMR with the finest wake-grid spacing or level-1 grid spacing equal to 10% C_{tip}, which matches the end spacing of the near-body grids. The outer boundaries of the Cartesian mesh are 20 rotor radii away from the origin. The off-body mesh has approximately 130 million grid points after numerical convergence.

The numerical setup of the current work is the as that of Jia et al. (Ref. 14). A fifth order spatial scheme and a second order implicit time marching scheme are implemented for both near-body and off-body CFD simulations. The turbulence model used in the present work is the Spalart-Allmaras RANS turbulence model coupled with Detached Eddy Simulation. A time step size of 0.25 degrees azimuth which results in 1,440 time steps per rotor revolution is used for the time-accurate simulations.

Acoustic Model

The software PSU-WOPWOP (Ref. 24) is a physics-based acoustic prediction tool developed at Penn State University. The software can predict discrete frequency and broadband rotor noise for arbitrary maneuvering flight. The code is a numerical implementation of Farassat's Formulation 1A (Ref. 25) of the Ffowcs Williams–Hawkings (FW-H) equation (Ref. 26). Formulation 1A can be written in a general form as:

$$p'(\vec{x},t) = p'_T(\vec{x},t) + p'_L(\vec{x},t) \tag{2}$$

where $p'_T(\vec{x},t)$ is the acoustic pressure due to the thickness noise contribution, and $p'_L(\vec{x},t)$ is the acoustic pressure due to the loading noise contribution. For this paper, only the loading noise is analyzed for the coaxial rotor system, and the loading noise can be written as

$$\begin{aligned} 4\pi p'_L(\vec{x},t) = & \frac{1}{c}\int_{f=0}\left[\frac{\dot{l}_r}{r|1-M_r|^2}\right]_{ret} dS + \\ & \int_{f=0}\left[\frac{l_r - l_M}{r^2|1-M_r|^2}\right]_{ret} dS + \\ & \frac{1}{c}\int_{f=0}\left[\frac{l_r(r\dot{M}_r + c(M_r - M^2))}{r^2|1-M_r|^3}\right]_{ret} dS \end{aligned} \tag{3}$$

where p' is the acoustic pressure; $f = 0$ defines the blade surface; ρ_0 and c are the density and speed of sound in the undisturbed medium (air), respectively; $r = |\vec{x} - \vec{y}|$ is the distance between the source position $\vec{y}$ and the observer position $\vec{x}$; $v_n = \vec{v} \cdot \hat{n}$ is the velocity of the surface $f = 0$ in the direction normal itself (i.e., $\hat{n}$ is an outward unit normal vector to the surface $f = 0$); M and M_r are the Mach number and Mach number component in the radiation direction of the surface $f = 0$, respectively; and l_r is the component of loading force that the surface imposes on the fluid, in the radiation direction.

The noise analysis performed by PSU-WOPWOP requires data on the blade geometry and loading. The geometry can be provided as either a lifting line or a distributed blade, and the loading as integrated loads or a pressure distribution. The CFD analysis is capable of providing distributed blade geometry as well as pressure, but the RCAS analysis can only provide integrated forces and lifting line geometry. In order to remain consistent in the analysis, the geometry is provided as a lifting line and the loading as the integrated forces along the lifting line.

RESULTS

This section analyzes the aeroacoustic results of the FWM, VPM, and CFD. In order to have consistency for the comparison, a single operating condition is analyzed using the three methods. The coaxial rotor system is trimmed to operate at 150 knots forward flight speed, 20% lift offset, and 0° shaft tilt.

This section is split into two subsections: aerodynamics and acoustics. The aerodynamics section analyzes the blade loads from the three methods while the acoustics subsection analyzes pertinent noise metrics.

Aerodynamics

In this section the blade loading and azimuthal derivative of loading are plotted and followed by plots of loading with respect to azimuth angle at specific radial sections.

Blade Loading The normal force is plotted in Fig. 2 as disk plots. The columns correspond to the analysis methods, and the rows the rotor (first row - upper rotor; second row - lower rotor). The rotor operates at 20% lift offset and therefore shows a higher concentration of loading on the advancing sides of the upper and lower rotors. This feature is captured by each model as seen by the low levels of loading on the retreating side (blue) and higher levels of loading on the advancing side (red). The more abrupt changes in blade loads (sharp changes in contour colors) is primarily due to impulsive aerodynamic interactions. And each of these methods of analysis captures these interactions differently. There are two primary interactions: blade-vortex interactions (BVI) and blade-crossover interactions (BCI). The BVI events occur when either a rotor ingests it owns wake (self-BVI) or when a rotor operates in another rotor's wake (rotor-to-rotor BVI). The BCI events occur when when the rotor blades of the upper and lower rotors cross one another. The BCI events can be seen on the retreating side of the upper rotor (240° and 300°).

Azimuthal Derivative of Loading In order to understand how the interactions are captured by the three models, the azimuthal derivative of normal force is analyzed. The derivative highlights regions of impulsive loading, and impulsive loading is generally a result of aerodynamic interactions (BVI and BCI events). The azimuthal derivative of normal force is plotted in Fig. 3 as disk plots. The rows and columns layout is the same as the previous plot, but the color range has been changed. The red and blue regions represent positive and negative derivative of loading, respectively. The white regions represent minimal to no change in loading. The retreating side of the rotors shows minimal changes in loading, and the majority of the interactions are concentrated on the advancing side of the rotors, with the exception of the CFD analysis. The CFD analysis captures two events at 240° and 300° azimuth on the upper rotor. These features extend from the root to the tip radially and also appear to some extend every 60°. These are the BCI events, and they are also evident on the lower rotor using CFD analysis, but not as prominent. The VPM analysis can also pick up these BCI interactions, but primarily on the advancing side of each rotor, and FWM analysis is unable to capture the 6/rev content. Apart from the BCI events, all three analysis methods capture BVI events predominantly on the advancing side of each rotor. The advancing side of the upper rotor shows three distinct BVI events from 0° to 90° for each analysis method. The location and intensity of the BVI events match well between VPM and CFD analysis, while the FWM analysis results in BVI events of higher intensity and slightly different locations compared to the two other methods. These same differences and similarities between the analysis methods are shown on the lower rotor. A feature prominent in only the CFD analysis, especially on the lower rotor, is the root BVI events to the rear of the rotor. These interactions occur due to the vortices shed at the root of the blade interacting with the rear of the rotor. A feature only captured by the FWM analysis are the radially extending lines near the root of the rotor disk. These occur 180° and 225°, as well as 315° to 360°. These features are likely not physically because the only interactions the FWM analysis would capture would be the wake interacting with the rotor. The CFD and VPM analysis can also capture wake-rotor interactions, but do not show these features in their loading plots. Thus, it would be reasonable to conclude these are non-physical features beacuse anything captured by the FWM should be captured by the VPM and CFD.

The main features captured by all three methods are the advancing side BVI events. The VPM and CFD analysis capture the BCI events, with the CFD analysis capturing retreating side BCI events on the upper rotor. And CFD also captures root BVI events not visible through the other analysis methods. Overall the VPM results seem to agree better with CFD, and FWM analysis shows differences in BVI location an intensity.

Span Analysis The plots analyzed thus far were disk plots of loading and the loading derivative. In order to analyze how much the loads and derivatives vary in magnitude, the plots are again analyzed at specific radial sections. The normal force and azimuthal derivative of normal force are plotted at 50%, 80%, and 90% span. Each figure contains four plots where two plots are the blade loads on the upper and lower rotors, and the two remaining plots are the azimuthal derivative of normal force. The blade loading plots are used to compare the loading magnitudes between the analysis methods. The plots of the derivative of loading are used to compare the intensity of the blade load fluctuations.

50% Span Analysis First, the loading at 50% span (Fig. 4) is analyzed. The figure contains four subplots in a two

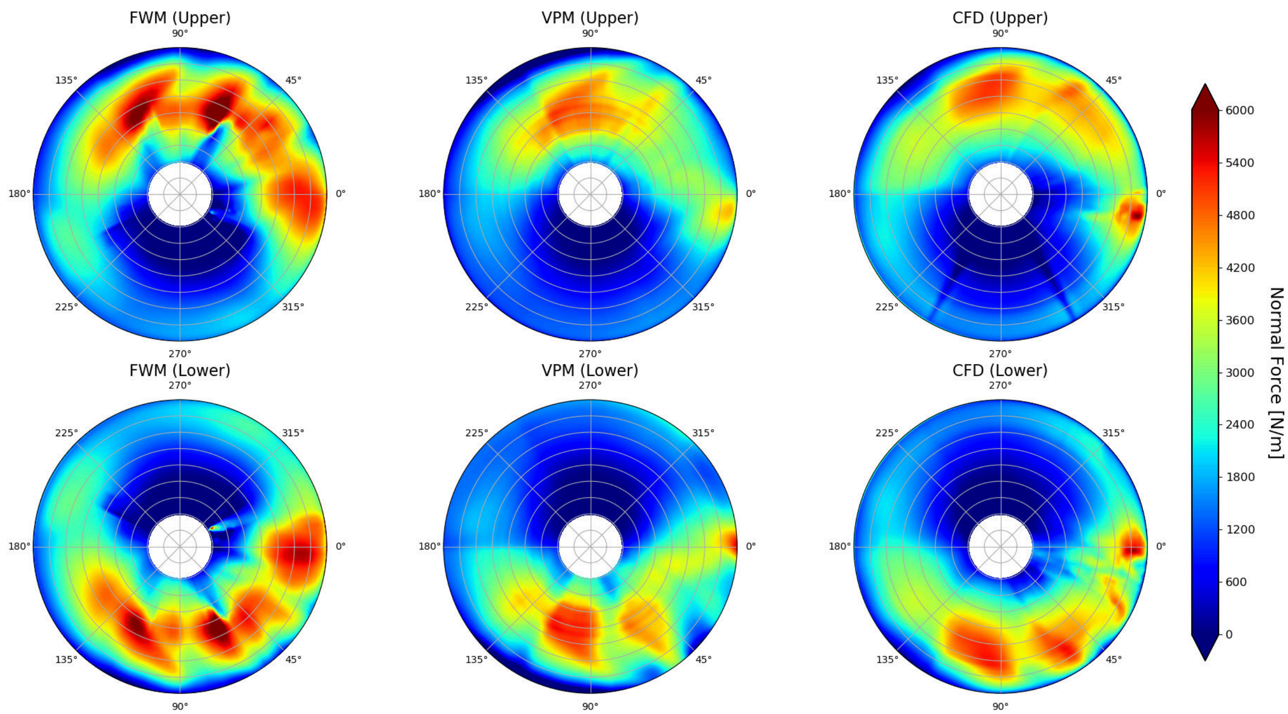

Fig. 2: Rotor normal force [N/m] on the upper rotor (first row) and lower rotor (second row) at 150 knots forward flight speed (moving right to left), 20% lift offset, and 0° shaft tilt.

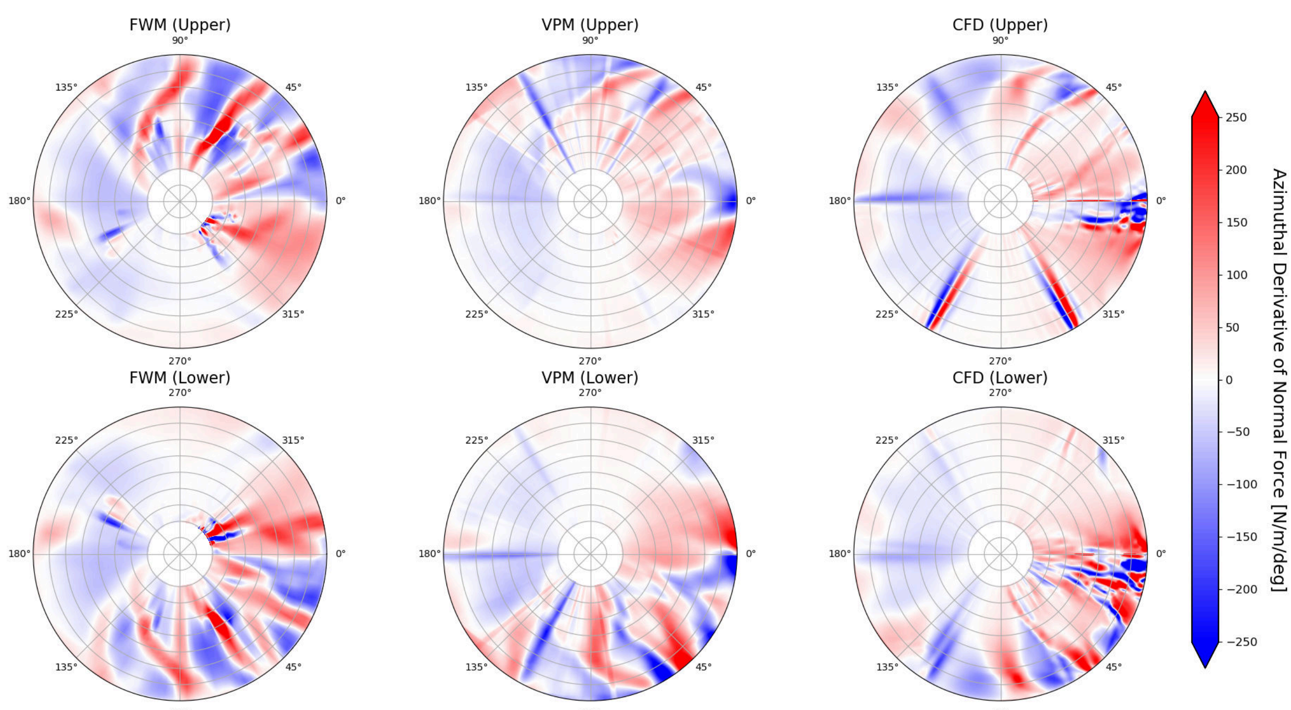

Fig. 3: Rotor azimuthal derivative normal force [N/m/deg] on the upper rotor (first row) and lower rotor (second row) at 150 knots forward flight speed (moving right to left), 20% lift offset, and 0° shaft tilt.

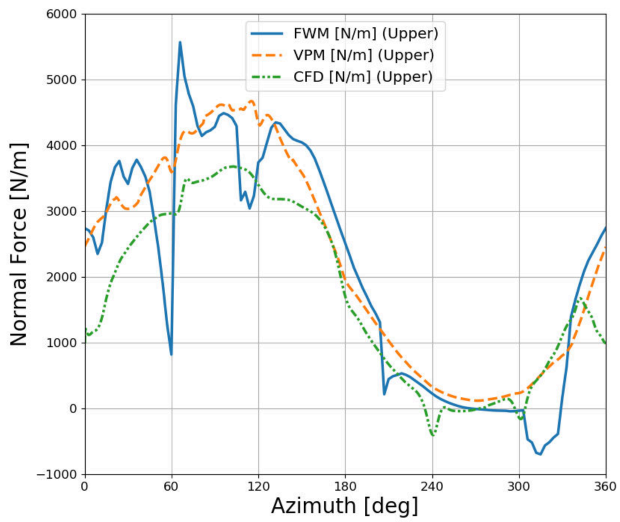

(a) Upper Rotor

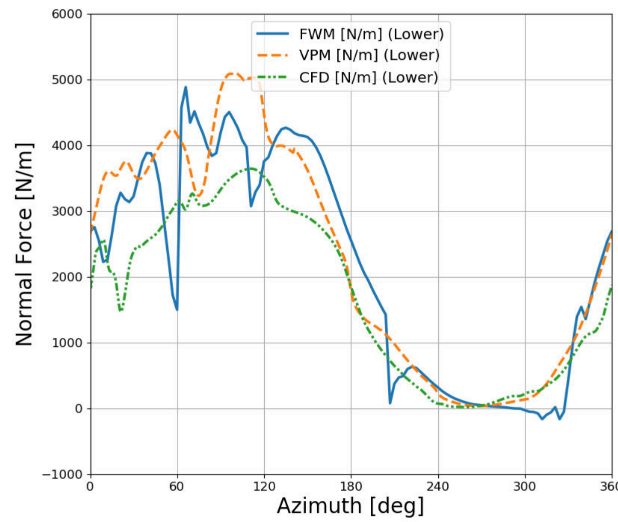

(b) Lower Rotor

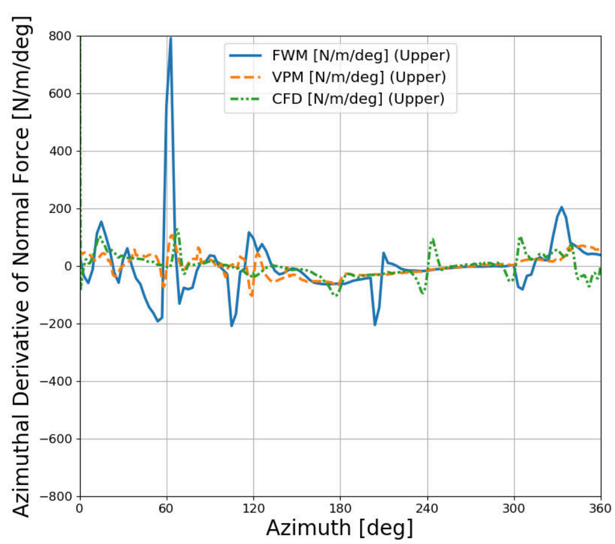

(c) Upper Rotor

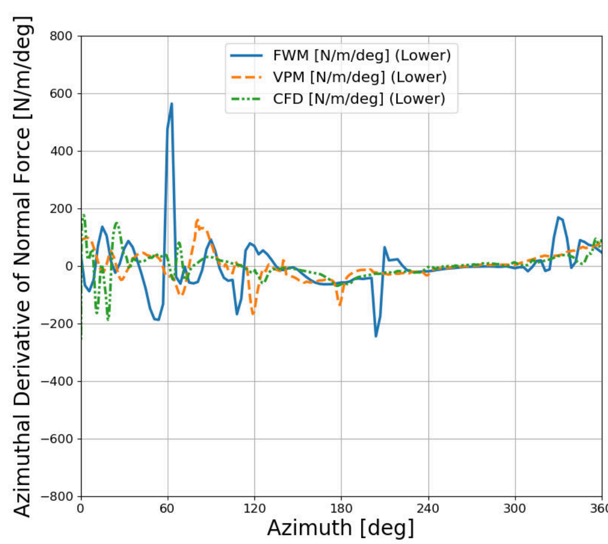

(d) Lower Rotor

Fig. 4: Normal force [N/m] and azimuthal derivative of normal force [N/m/deg] at 50% span.

by two layout. Each plot contains three lines corresponding to FWM, VPM, and CFD results. The first row is the normal force and the second row is the azimuthal derivative of normal force, and the first column corresponds to the upper rotor results and the second column the lower rotor results. The upper rotor normal force at 50% (Fig. 4a) shows similarities in waveforms between the analysis methods, but with distinguishing features. The VPM and CFD results compare well, but the VPM results over-predict loads on the advancing side relative to the CFD results. The CFD results also show negative peaks at 240° and 300° which are not shown in the VPM results (BCI events discussed previously). The FWM results show the greatest discrepancies compared to CFD. On the advancing and retreating sides of the rotor, the FWM results show a large change in loading not predicted by the other two methods. On the advancing side those changes are BVI events, but much more intense than anything experienced by VPM or CFD. On the retreating side, the FWM results also show fluctuations, but these are the same features discussed from Fig. 3 near the root. And these features are likely non-physical. The derivative of loading for the upper rotor (Fig. 4c) show fluctuations on the advancing side of the rotor, but the FWM results have much more intense BVI events, while the CFD and VPM results match more closely. Again, a major difference between CFD and the two other methods is the BCI events which are evident at 240° and 300°. The lower rotor results (Fig. 4d) also show similar trends with one difference being the fluctuations between 0° and 60° azimuth for the CFD results. These fluctuations are due to the root BVI events captured by CFD.

80% Span Analysis Analysis is also performed further outboard at 80% span and plotted in Fig. 5. The blade loads for the upper and lower rotors (Fig. 5a and 5b) show better waveform agreement between VPM and CFD than with FWM. The primary peaks for VPM and CFD line up well (with the exception of the upper rotor BCI events), but the loads on the advancing side have a difference in loading magnitude. The FWM results show more loading peaks on the advancing side compared to VPM and CFD. The BCI events on the retreating side of the upper rotor for CFD analysis show narrower peaks compared to the analysis at 50% span (likely due to the higher rotational rates outbaord). The azimuthal derivative results (Fig. 5c and 5d) show good agreement between CFD and VPM. The FWM results show fluctuations that are offset from CFD on the advancing side. The CFD BCI events and root BVI events are more intense further outboard, and should results in discrepancies between the acoustic results compared to the FWM and VPM acoustic results. This would be due to the loading noise being dependent on the rate of change in loading, and if CFD is predicting time varying features which VPM and FWM are not, CFD would likely show differences in magnitude and directionality in the noise results.

90% Span Analysis Analysis at 90% span (Fig. 6) also show that the VPM results continue to match better with CFD in regards to waveform. Except for the omission of the root BVI events and BCI events at the retreating side of the upper rotor. The FWM results show BVI events but the events do not agree as well in location with CFD as do the VPM results.

Summary These line plots show that FWM results further inboard show the greatest difference with CFD and VPM in regards to the intensity and location of the BVI events. Further outboard the FWM BVI events agree better with CFD and VPM analysis as the intensity of the interactions reduces, but the locations of the interactions continue to show differences. There are also non-physical features captured on the retreating side of the FWM results which do not appear in the CFD and VPM analysis. The VPM azimuthal derivative of loading results agree well with CFD results, but the CFD results predict BCI events on the retreating side of the upper rotor and root BVI events on the rear of the lower rotor. And these features are not accounted for by the FWM and VPM analysis. The next section will analyze how these interactions captured by the three methods impact the noise of the rotor system.

Acoustics

In this section the results from the three analysis methods in the previous section are again analyzed for their influence on rotor noise. The impulsive loading sources (BVI and BCI) are dominant sources of loading noise as shown in Eqn. 3. The term l_r is a dominant near-field term and $\dot{l}_r$ is a dominant far field term, the loading in the radiation direction and the time derivative of loading in the radiation direction, respectively. As the magnitude and the intensity of the impulsive load sources increases, so do these terms, and therefore the noise.

Noise Hemisphere Plots The noise from the rotor system is measured on a hemisphere surrounding the rotor system. The hemisphere moves in the same direction and at the same speed as the rotor. Thus the relative position of the hemisphere and the rotor system remains constant. The spherical grid has 120 points in the azimuthal direction and 60 points in the elevation direction for a total of 7200 points and each point is 10 rotor radii from the origin, which is situated at the hub of the lower rotor. The azimuth angle ranges from 0° to 360° (0° downstream from the rotor and 90° on the starboard side of the rotor) and elevation angle ranges from 0° to -90° (0° in plane of the rotor system and -90° directly below the rotor system). The hemisphere is displayed in an isometric view as well as a top view in Fig. 7 with +x-direction pointing ahead of the rotor system and +y-direction pointing to the starboard side.

The noise metric computed at each point on the grid is the mid-frequency sound pressure level (midSPL), which is an integrated noise measurement that includes the sound pressure levels in the frequency range of the 10th to 50th rotor harmonics. The purpose of filtering the noise to a specific frequency range is to capture higher frequency noise content where BVI and BCI noise is more prevalent. The hemisphere plots of

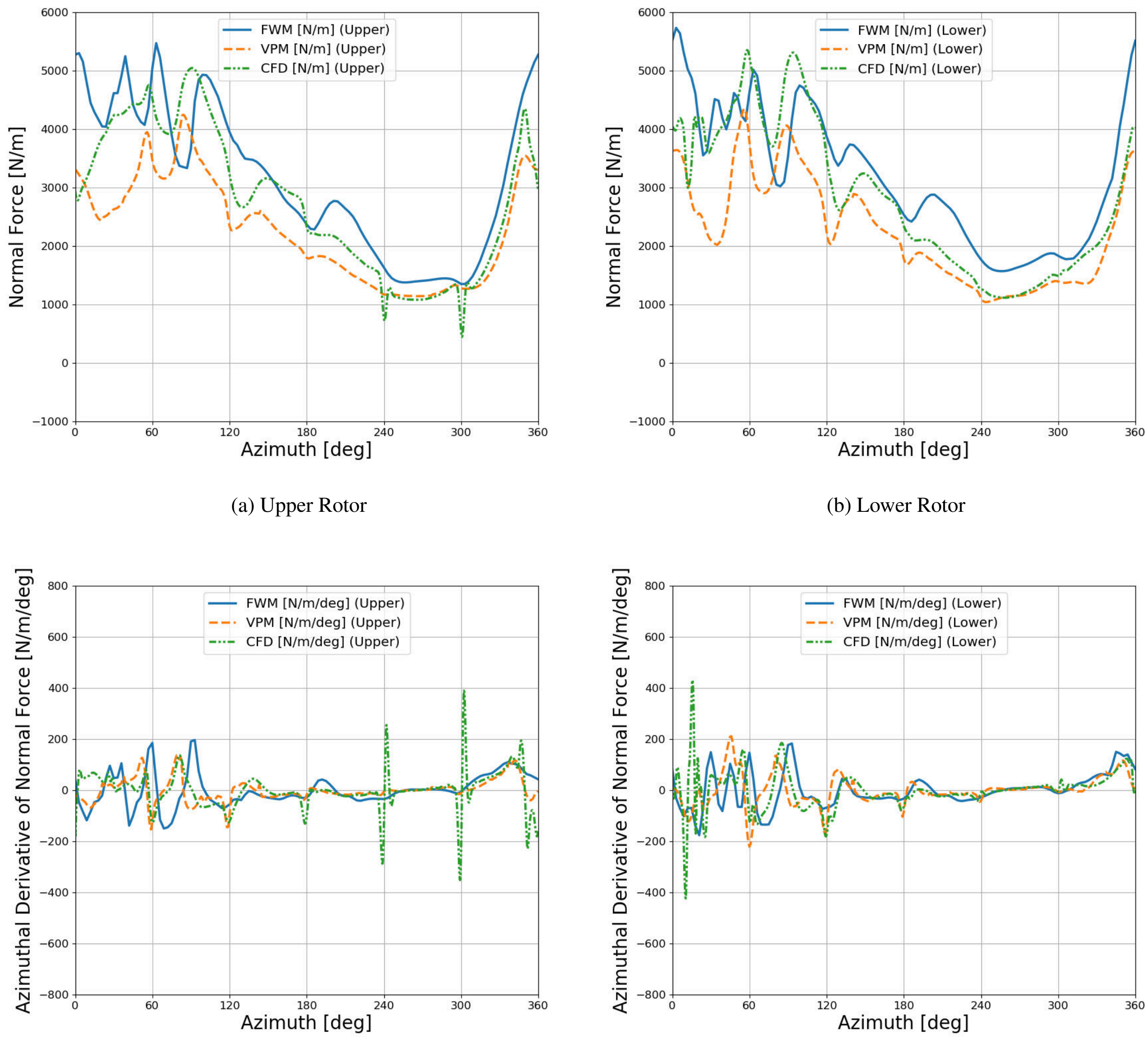

(a) Upper Rotor

(b) Lower Rotor

(c) Upper Rotor

(d) Lower Rotor

Fig. 5: Normal force [N/m] and azimuthal derivative of normal force [N/m/deg] at 80% span.

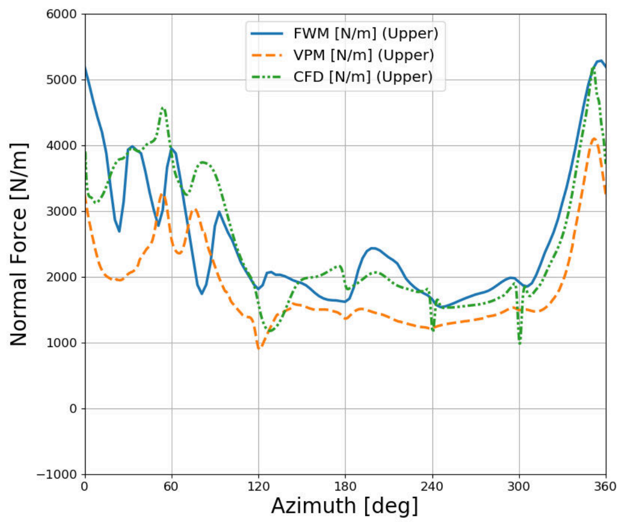

(a) Upper Rotor

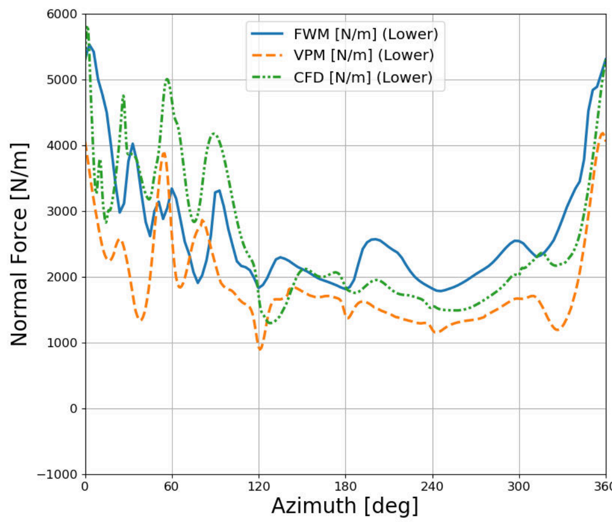

(b) Lower Rotor

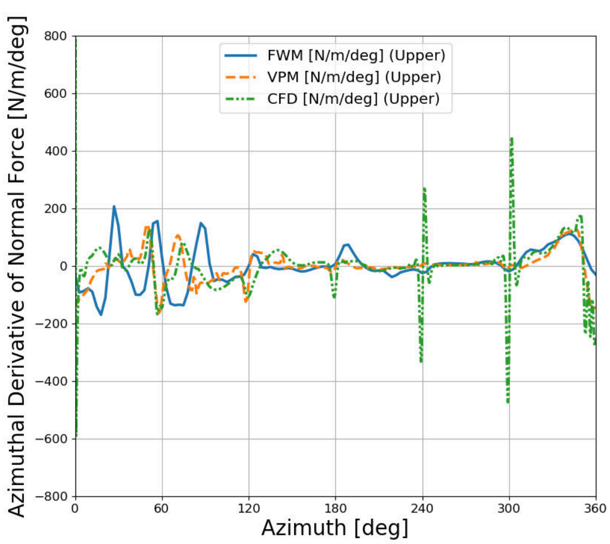

(c) Upper Rotor

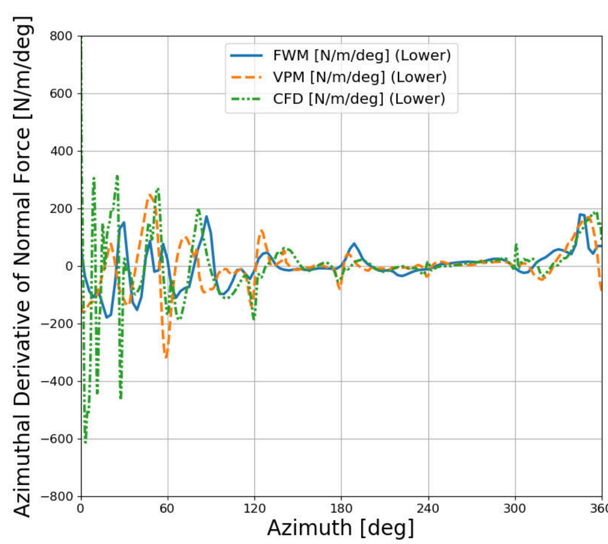

(d) Lower Rotor

Fig. 6: Normal force [N/m] and azimuthal derivative of normal force [N/m/deg] at 90% span.

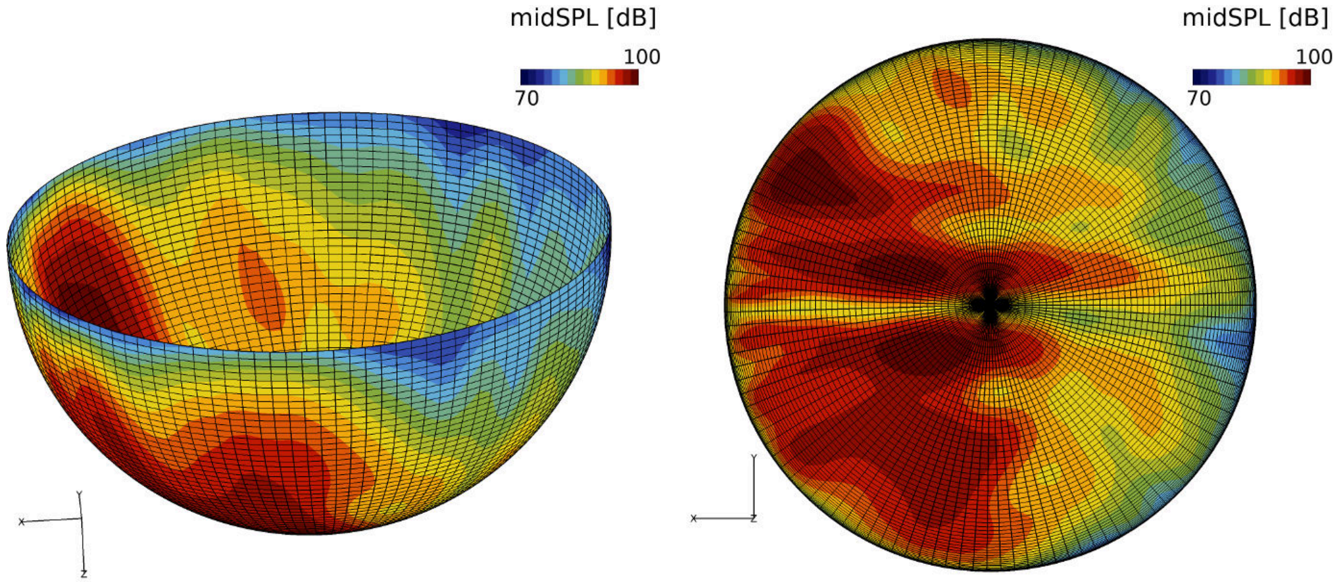

(a) Isometric view.

(b) Top view.

Fig. 7: midSPL on hemisphere with forward motion in +x-direction and starboard in +y-direction.

midSPL are shown in Fig. 8 in a three by three grid. Each row corresponds to a different analysis method (first row - FWM; second row - VPM; third row - CFD) and each column corresponds to a different noise source (first column - coaxial rotor system; second column - upper rotor; third column - lower rotor). The plots of the individual rotor noise contains either a white cross, or a white and black cross. The lines of the cross intersect at a point of high noise, and these points are further analyzed later in the section. The white cross is referred to as point 1, and the black cross as point 2.

The purpose of splitting the coaxial rotor noise into its rotor components is to better understand the source of the noise. For example, in the plot in Fig. 8a it is not clear which rotor is contributing to which region of noise, and the greatest noise is concentrated ahead of the rotor system. Looking at the plots of the noise from the individual rotors in Fig. 8b and 8c provides more clarity. The upper rotor contributes to the noise starboard of the rotor system and the lower rotor to the port side of the rotor system. The VPM (Fig. 8d) noise plot is similar to the FWM noise plot, but analyzing the individual rotor noise results show differences in noise directivity. The upper (Fig. 8e) and lower (Fig. 8f) rotor noise results show two high-noise regions each ahead of the rotor. The CFD coaxial rotor noise hemisphere (Fig. 8g shows high levels of noise to the port and rear. The individual rotor contributions show that the upper rotor is the primary contributor to the rearward noise and the lower rotor contributes to the noise on the port and in the front of the rotor system. The individual rotor noise hemisphere plots have either a white or black cross, or both. These crosses specify regions of high noise which are analyzed later in this section.

FWM Hemisphere Analysis The crosses on the individual rotor hemisphere plots in Fig. 8b and 8c are analyzed further in Fig. 9. Each row corresponds to a specific cross on the FWM hemisphere noise plots. The first row is for the analysis of point 1 (white cross on Fig. 8b). The first column is the loading acoustic pressure at point 1 (Fig. 9a) for the upper rotor. The plot is the loading acoustic pressure at an observer time range for a single rotor revolution. The pressure plot has 3/rev content because the rotor is 3-bladed. A single peak is selected and highlighted by a red dashed-dotted box along with an associated observer time range which encompasses the peak. The second column is the loading disk plot (Fig. 9b) along with the rotor blade positions at the observer times specified in the acoustic pressure plot. The blades are warped because they are not plotted where they are when the observer hears the noise, but where each blade segment was when it omitted the noise. There are also 6 blades because the plot is of the 3 blades at the start of the observer time for the highlighted pressure range and at the end of the range. The third column is the disk plot of the loading noise integrand (Fig. 9c). The loading noise integrand is the summation of the integrand from Eqn. 3, and the integration of the integrand over the blade span results in the acoustic pressure. The noise at point 1 from the upper rotor is primarily due to the BVI event on the advancing side. The second row in Fig. 9 corresponds to the analysis of point 1 of the lower rotor in Fig. 8c. Just as the upper rotor noise analysis, the region of high noise of the lower rotor is also due to the advancing side BVI.

VPM Hemisphere Analysis The plots for the analysis of the VPM regions of high noise are shown in Fig. 10. The first row (Fig. 10a, 10b, and 10c) analyzes point 1 (white cross in Fig. 8e) of the upper rotor. The peak acoustic pressure is due to the

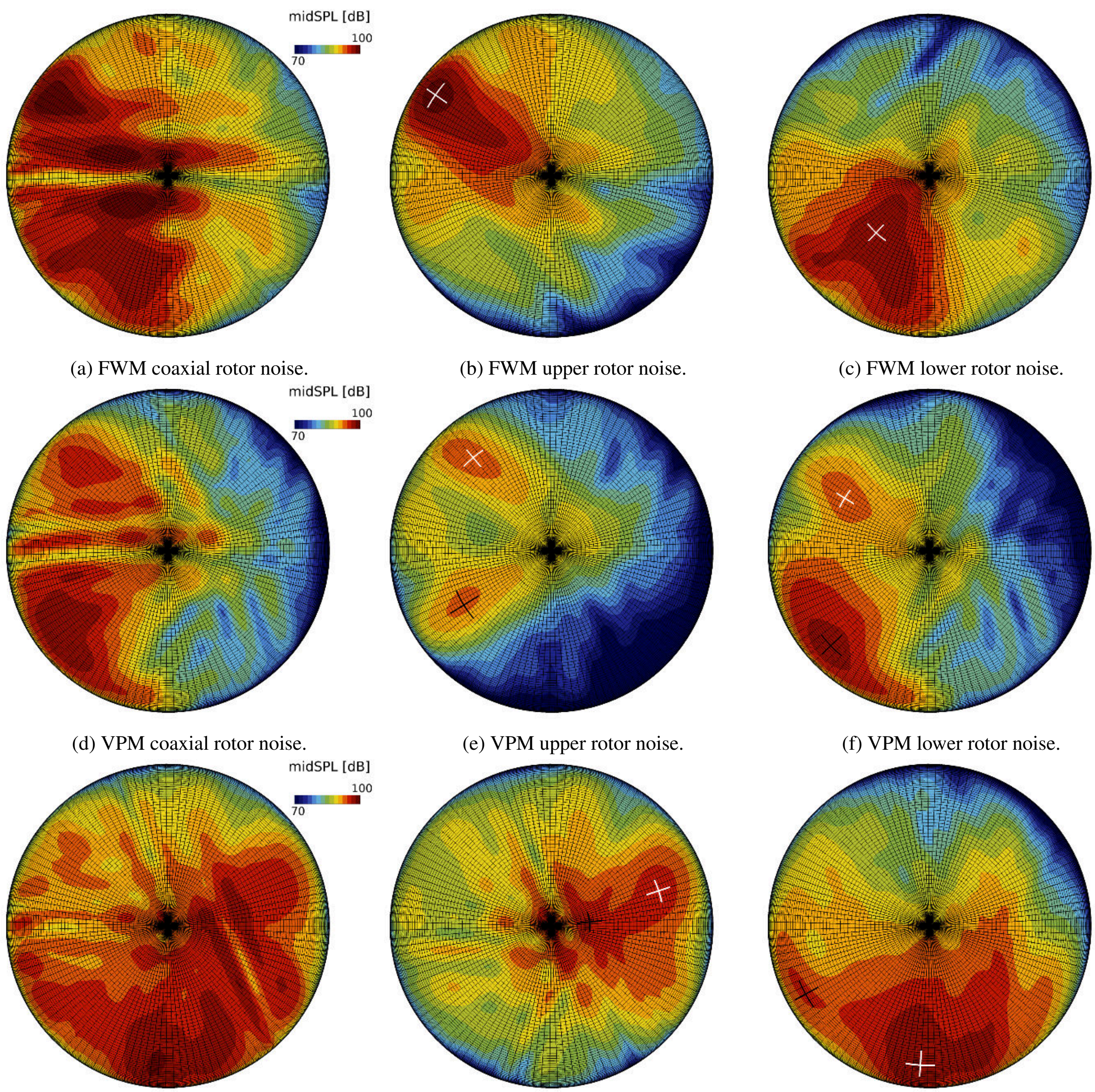

(a) FWM coaxial rotor noise. (b) FWM upper rotor noise. (c) FWM lower rotor noise.

(d) VPM coaxial rotor noise. (e) VPM upper rotor noise. (f) VPM lower rotor noise.

(g) CFD coaxial rotor noise. (h) CFD upper rotor noise. (i) CFD lower rotor noise.

Fig. 8: Hemisphere of OASPL between the 10th and 50th rotor harmonics (midSPL) due to the coaxial rotor system, upper rotor, and lower rotor measured 10 rotor radii from the rotor center for FWM, VPM, and CFD analysis (white cross - point 1; black cross point 2.

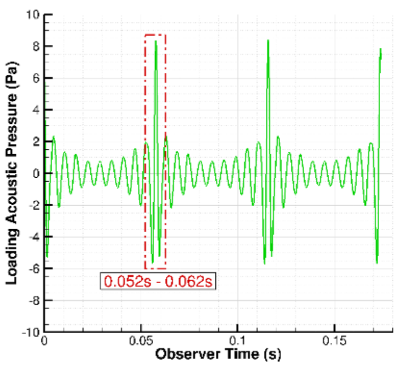

(a) Acoustic pressure.

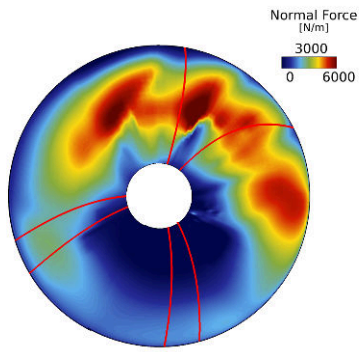

(b) Normal force.

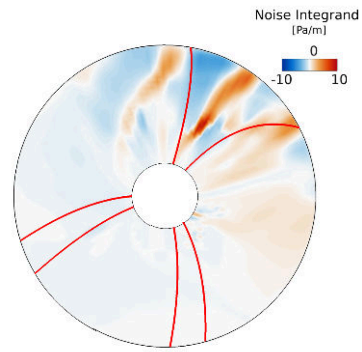

(c) Loading noise integrand.

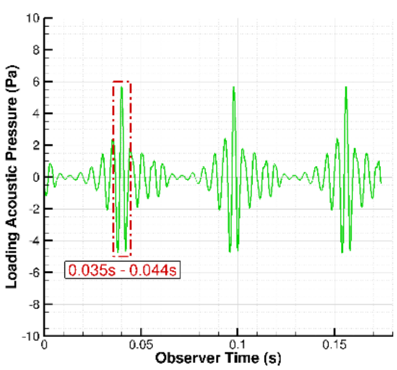

(d) Acoustic pressure.

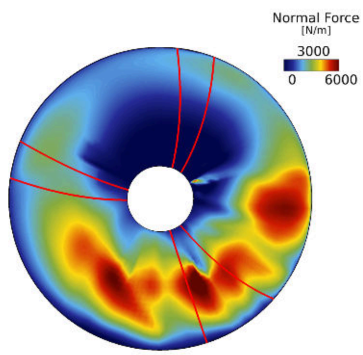

(e) Normal force.

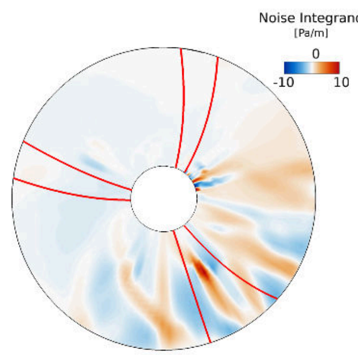

(f) Loading noise integrand.

Fig. 9: FWM upper rotor (first row - point 1) and lower rotor (second row - point 1) noise hotspot results.

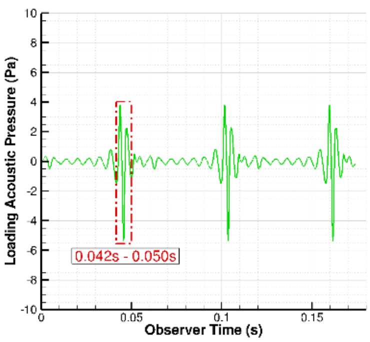

(a) Acoustic pressure.

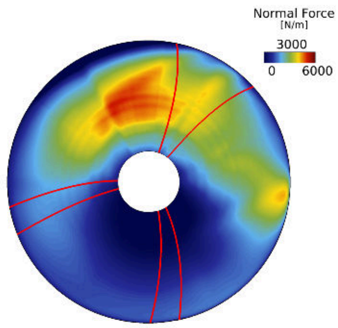

(b) Normal force.

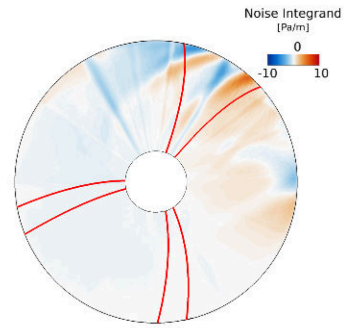

(c) Loading noise integrand.

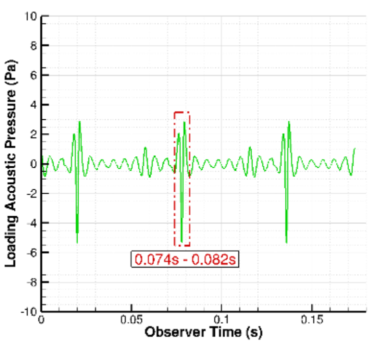

(d) Acoustic pressure.

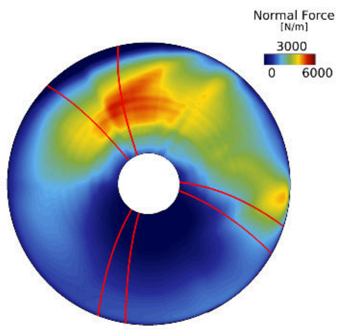

(e) Normal force.

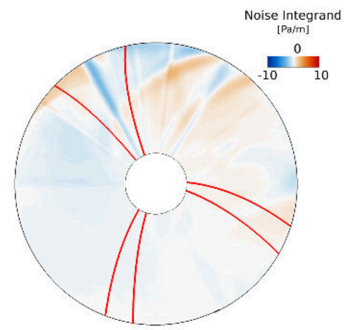

(f) Loading noise integrand.

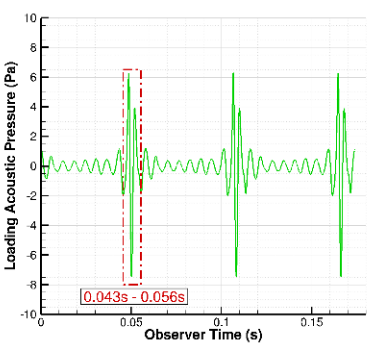

(g) Acoustic pressure.

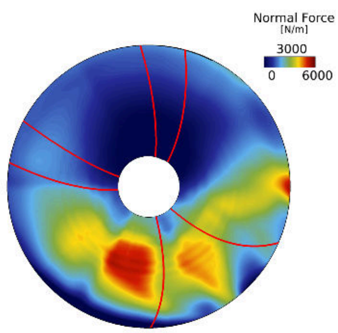

(h) Normal force.

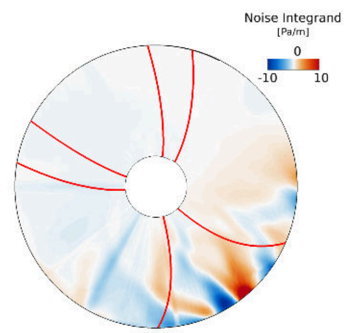

(i) Loading noise integrand.

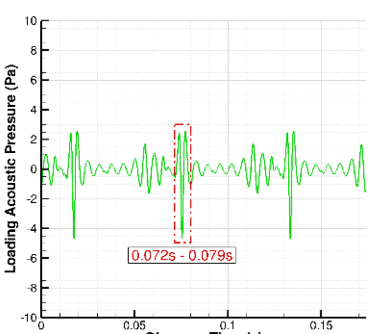

(j) Acoustic pressure.

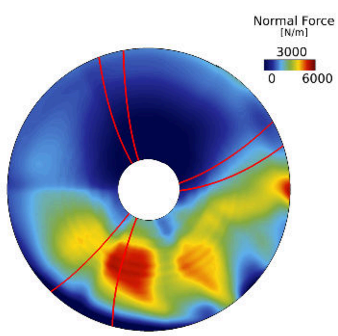

(k) Normal force.

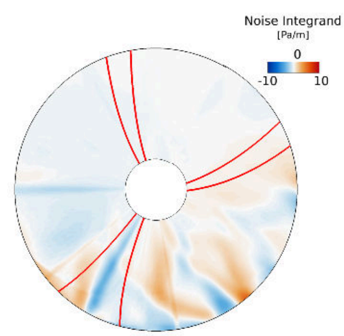

(l) Loading noise integrand.

Fig. 10: VPM upper rotor (first row - point 1; second row - point 2) and lower rotor (third row - point 1; fourth row - point 2) noise hotspot results.

BVI events on the advancing side of the rotor. For the analysis of point 2 (black cross in Fig. 8e) the second row (Fig. 10d, 10e, and 10f) is referenced. For point 2 the BCI event on the advancing side of the rotor is responsible. The lower rotor shows similar trends to the upper rotor. The third row plots (Fig. 10g, 10h, and 10i) and the fourth row plots (Fig. 10j, 10k, and 10l) are used to analyze point 1 (white cross in Fig. 8f) and point 2 (black cross in Fig. 8f), respectively. Just as the upper rotor noise analysis, the two regions of high noise from the lower rotor are due to the the BVI and BCI events on the advancing side.

CFD Hemisphere Analysis The plots for the analysis of the regions of high noise using CFD are shown in Fig. 11. The first row (Fig. 11a, 11b, and 11c) corresponds to point 1 in Fig. 8h. This point is further to the rear of the rotor and the acoustic pressure (Fig. 11a) shows two repeating peaks. This first peak is outline by the red box, and the second peak is highlighted by a black dashed-dotted-dotted box. On the blade loading plot (Fig. 11b) the color of the blades correspond to the colors of the boxes which enclose the peaks in the acoustic pressure plot. The first peak is due to the BCI event at 300°, and the second peak is due to the root BVI at 0°. The second row (Fig. 11d, 11e, and 11f) correspond to point 2 of the noise hemisphere plot of the upper rotor (Fig. 8h). The first acoustic pressure peak (Fig. 11d) is due to the BCI event at 300°. The second acoustic pressure peak highlighted by the black box is due to the BCI event at 240° and the root BVI event at 0°. The third row (Fig. 11g, 11h, and 11i) corresponds to point 1 on the noise hemisphere plot of the lower rotor (Fig. 8i). The pressure peak in Fig. 11g is due to the root BVI event. The fourth row (Fig. 11j, 11k, and 11l) corresponds to point 2 on the noise hemisphere plot of the lower rotor (Fig. 8i). The first pressure peak in Fig. 11j is due to the root BVI event, and the second peak is due to the advancing side BVI.

Summary The FWM and VPM analysis acoustic hemisphere results show high levels of noise to the front of the rotor. While the FWM results are primarily due to only the BVI events, the VPM results are due to the advancing side BCI and BVI events. Even though there are two sources of impulsive noise from the VPM analysis, the FWM coaxial rotor noise results are on par and/or even higher. This is because the inboard BVI events from the FWM analysis are more intense than the BVI events from VPM or CFD analysis. CFD analysis shows higher noise levels to the port side and rear side of the rotor system. The noise to the rear and the port side are due to the root BVI events and the BCI events on the retreating side of the upper rotor.

CONCLUDING REMARKS

In this paper aeracoustic analysis was performed using the FWM, VPM, and CFD. Analysis was performed on a coaxial rotor system operating at 150 knots forward flight speed, 20% lift offset, and 0° shaft tilt. The paper first explored the blade loads and the derivative of loading from the three analysis methods. After, noise analysis is performed on a hemisphere grid surrounding the rotor system. The major noise sources are the BVI and BCI events, and the manner in which the analysis methods capture these interactions led to differences between the results.

The main features captured by all three methods are the advancing side BVI events. The VPM and CFD analysis capture the BCI events, with the CFD analysis capturing retreating side BCI events on the upper rotor. And CFD also captures root BVI events not visible through the other analysis methods. Overall the VPM results seem to agree better with CFD, and FWM analysis shows differences in BVI location an intensity. Analysis at specific radial stations show that the FWM results further inboard have the greatest difference in comparison with the CFD and VPM results in regards to the intensity and location of the BVI events. Further outboard the FWM BVI events agree better with CFD and VPM analysis as the intensity of the interactions reduces, but the locations of the interactions continue to show differences. There are also non-physical features captured on the retreating side of the FWM results which do not appear in the CFD and VPM analysis. The VPM azimuthal derivative of loading results agree well with CFD results, but the CFD results predict BCI events on the retreating side of the upper rotor and root BVI events on the rear of the lower rotor. And these features are not accounted for by the FWM and VPM analysis. The next section will analyze how these interactions captured by the three methods impact the noise of the rotor system.

The FWM and VPM analysis acoustic hemisphere results show high levels of noise to the front of the rotor. While the FWM results are primarily due to only the BVI events, the VPM results are due to the advancing side BCI and BVI events. Even though there are two sources of impulsive noise from the VPM analysis, the FWM coaxial rotor noise results are on par and/or even higher. This is because the inboard BVI events from the FWM analysis are more intense than the BVI events from VPM or CFD analysis. CFD analysis shows higher noise levels to the port side and rear side of the rotor system. The noise to the rear and the port side are due to the root BVI events and the BCI events on the retreating side of the upper rotor.

Overall, the VPM and CFD analysis showed the best agreement in regards to blade loading analysis. But the FWM and VPM acoustic results show greater agreement because the root BVI events and the upper rotor's retreating side BCI events for the CFD analysis result in noise to the port and rear side of the rotor system. These root BVI and BCI events of the CFD analysis result in the greatest variation in noise directivity and intensity compared to the other two methods and should be addressed.

For future work three areas should be addressed. First, the BCI events and root BVI events are the primary causes of the differences between the CFD results compared with the other

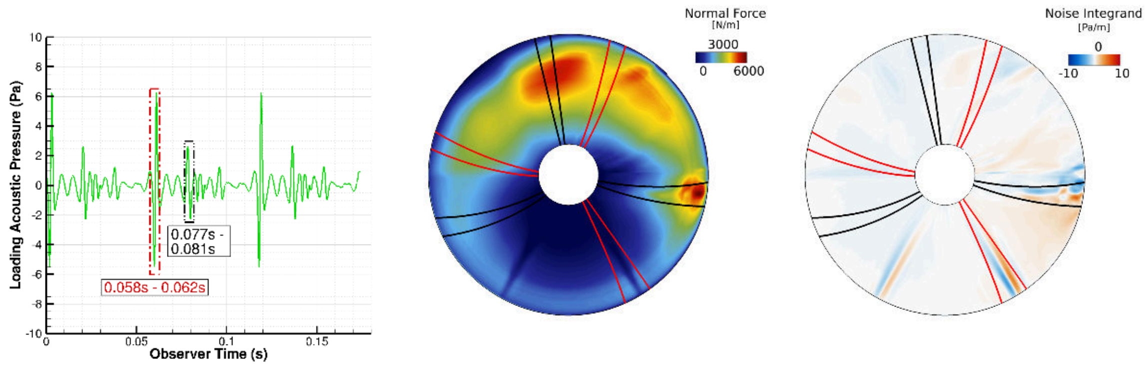

(a) Acoustic pressure. (b) Normal force. (c) Loading noise integrand.

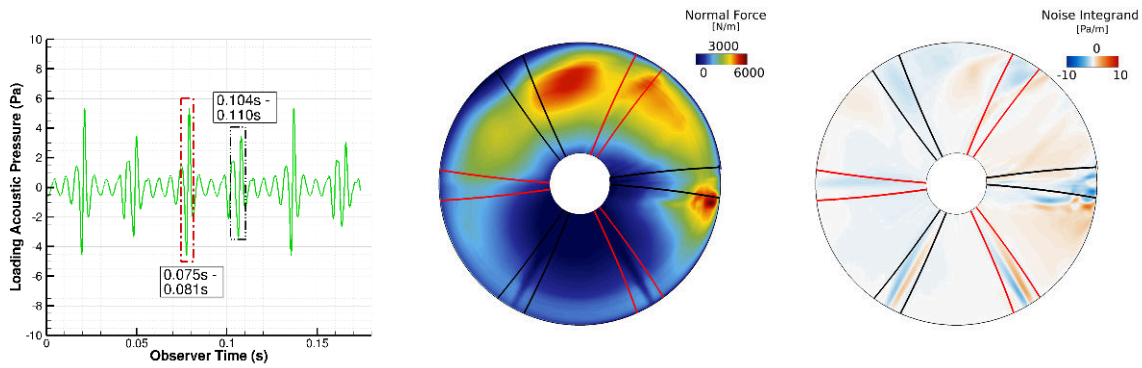

(d) Acoustic pressure. (e) Normal force. (f) Loading noise integrand.

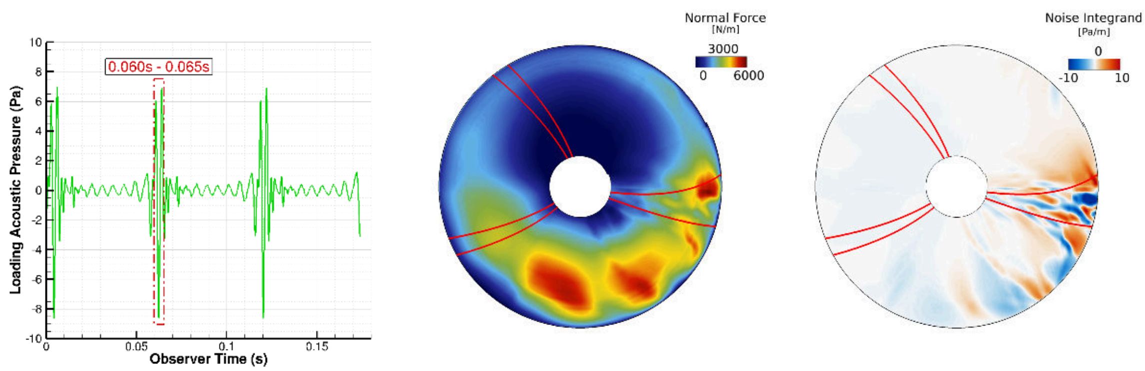

(g) Acoustic pressure. (h) Normal force. (i) Loading noise integrand.

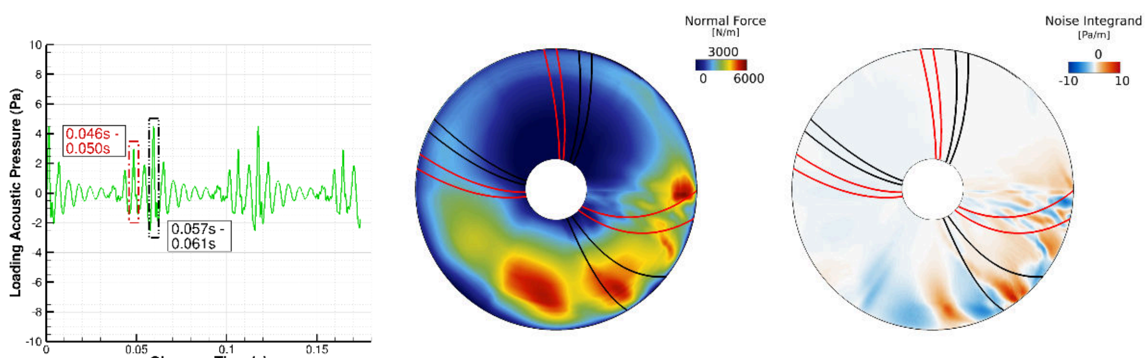

(j) Acoustic pressure. (k) Normal force. (l) Loading noise integrand.

Fig. 11: CFD upper rotor (first - point 1; second row - point 2) and lower rotor (third row - point 1; fourth row - point 2) noise hotspot results.

two methods. In order to have better comparison it would be worthwhile to account for these interactions in the other two methods in the future. Second, though this paper did not directly address the mathematical differences in the fundamental equations resulting in the differences in the analysis, it would be valuable for future research endeavours to perform this analysis. Third, only a single operating condition was analyzed in this paper. Perhaps in other conditions these interactions are not as important and may lead to better agreement between the analysis methods. Therefore, more operating conditions should be explored in order to widen the scope of the research.

ACKNOWLEDGMENTS

Through VLRCOE, this research was partially funded by the Government under Agreement No. W911W6-17-2-0003. The U.S. Government is authorized to reproduce and distribute reprints for Government purposes notwithstanding any copyright notation thereon. The views and conclusions contained in this document are those of the authors and should not be interpreted as representing the official policies, either expressed or implied, of the Aviation Development Directorate or the U.S Government.

Research was sponsored by the Army Research Laboratory and was accomplished under Cooperative Agreement Number W911NF-20-2-0013. The views and conclusions contained in this document are those of the authors and should not be interpreted as representing the official policies, either expressed or implied, of the Army Research Laboratory or the U.S. Government. The U.S. Government is authorized to reproduce and distribute reprints for Government purposes notwithstanding any copyright notation herein.

The author would like to thank the High-Performance Internship Program (HIP) for providing funding and resources.

REFERENCES

[1]Ruddell, A.J., “Advancing Blade Concept (ABC^{TM}) Development,” 32nd Annual National Forum of the American Helicopter Society, May 1976.

[2]Hirschberg, M., “JMR Technology Demonstration Update: The Road to Future Vertical Lift,” *Vertiflite*, Vol. 62, N. 1, January/February 2016, pp. 22-27.

[3]Ruddell, A. J., Groth, W., McCutcheon, R., “The Advancing Blade Concept (ABC) Technology Demonstrator,” United States Army Research and Technology Labratories (AVRADCOM), April 1981.

[4]Boyd, D., Burley, C., and Conner, D., “Acoustic Predictions of Manned and Unmanned Rotorcraft Using the Comprehensive Analytical Rotorcraft Model for Acoustics (CARMA) Code System,” American Helicopter Society International Specialists’ Meeting on Unmanned Rotorcraft, Chandler, AZ, January 2005.

[5]Wachpress, D. A. and Quackenbush, T. R., “Impact of Rotor Design on Coaxial Rotor Performance, Wake Geometry, and Noise,” American Helicopter Society 62nd Annual Forum, Montréal, 29 April - May 1, 2008.

[6]Kim, W. H., Brown, R.E., and Duaraisamy, K., “Effect of Rotor Stiffness and Lift Offset on the Aeroacoustics of a Coaxial Rotor in Level Flight,” American Helicopter Society 65th Annual Forum, Grapevine, TX, 27-29 May 2009.

[7]Brown, R.E., Line, A.J., ”Efficient High-Resolution Wake Modeling Using the Vorticity Transport Equation,” *AIAA Journal*, Vol. 43, No. 7, April 2005, pp. 1434-1443.

[8]Walsh, G., Brentner, K.S., Jacobellis, and G., Gandhi, F., “An Acoustic Investigation of a Coaxial Helicopter in High-Speed Flight,” American Helicopter Society 72nd Annual Forum, West Palm Beach, FL, May 17-19, 2016.

[9]Barbley, N. L., Komerath, N. M., Novak L. A., “A Study of Coaxial Rotor Performance and Flow Field Characteristics,” 2016 AHS Technical Meeting on Aeromechanics Design for Vertical Lift, Fisherman’s Wharf, San Francisco, CA January 20-22, 2016.

[10]Herrmann, T. A., Celi, R., and Baeder, J. D., “Multidisciplinary Trim Analysis of a Coaxial-Pusher Rotorcraft Configuration,” American Helicopter Society 74th Annual Forum, Phoenix, AZ, May 14-17 2018.

[11]Klimchenki, V., Sridharan, A., and Baeder, J., “CFD/CSD Study of the Aerodynamic Interactions of a Coaxial Rotor in High-Speed Forward Flight,” 35th AIAA Applied Aerodynamics Conference, Denver, Colorado, June 5-9, 2017.

[12]Jia, Z., Lee, S., Sharma., K., and Brentner, K. S., “Aeroacoustic Analysis of a Lift-Offset Coaxial Rotor Using High-Fidelity CFD-CSD Loose Coupling Simulation,” American Helicopter Society 74th Annual Forum, Phoenix, AZ, May 14-17, 2018.

[13]Jacobellis, G., Anusonti-Inthra, P., and Gandhi, F., “Investigation of Blade Loads on a Modern High-Speed Lift-Offset Coaxial Helicopter using Coupled Computational Fluid Dynamics/Computational Structural Dynamics,” Aeromechanics Design for Transformative Vertical Flight & The 5th Transformative Vertical Flight Workshop, San Francisco, CA, Jan. 16-19, 2018.

[14]Jia, Z., Lee, S., Sharma., K., and Brentner, K. S., “Effect of Pitch Attitude on the Performance and Acoustics of a Lift-Offset Coaxial Rotor Based on High-Fidelity CFD/CSD Simulations,” Vertical Flight Society 75th Annual Forum & Technology Display, Philadelphia, PA, May 13-16, 2019.

[15]Saberi, H., Khoshlahjeh, M., Ormiston, R. A., and Rutkowski, M. J., “Overview of RCAS and Application to Advanced Rotorcraft Problems,” Proceedings of the American Helicopter Society 4th Decennial Specialists’ Conference on Aeromechanics, San Francisco, CA, January 21–23, 2004.

[16]Jacobellis, G., Gandhi, F., and Floros, M., "Using Control Redundancy for Power and Vibration Reduction on a Coaxial Helicopter at High Speeds," Journal of the American Helicopter Society, Vol. 64, (032008), 2019.

[17]Wissink, A., Potsdam, M., Jain, R., Leffell, J., Jayaraman, B., Roget, B., Lakshminaravan, V., Forsythe, J., Sitaraman, J., and Bauer, A., "Improvements in the Helios Rotorcraft Simulation Code," American Helicopter Society 72nd Annual Forum, West Palm Beach, Florida, May 17–19, 2016.

[18]Felker III, F. F., "Performance and Loads Data from a Wind Tunnel Test of a Full-Scale, Coaxial, Hingeless Rotor Helicopter," NASA TM-81329, Oct. 1981.

[19]He, C., and Zhao, J., "Modeling Rotor Wake Dynamics with Viscous Vortex Particle Method," AIAA Journal, vol. 47, no. 4, pp. 902–915, 2009

[20]Wissink, A., Potsdam, M., Jain, R., Leffell, J., Jayaraman, B., Roget, B., Lakshminaravan, V., Forsythe, J., Sitaraman, J., and Bauer, A., "Improvements in the Helios Rotorcraft Simulation Code," American Helicopter Society 72nd Annual Forum, West Palm Beach, Florida, May 17–19, 2016.

[21]Potsdam, M., Yeo, Hyeonsoo, and Johnson, W., "Rotor Airloads Prediction Using Loose Aerodynamic/Structural Coupling," *Journal of Aircraft*, Vol. 43, (3), May–June 2006, pp. 732–742.

[22]Nichols, R., Tramel, R., and Buning, P., "Solver and Turbulence Model Upgrades to OVERFLOW 2 for Unsteady and High-Speed Flow Applications," AIAA 25th Applied Aerodynamics Conference, San Francisco, California, June 5–8, 2006.

[23]Hornung, R. D., A. M. Wissink, and S. R. Kohn, "Managing Complex Data and Geometry in Parallel Structured AMR Applications," Engineering with Computers, Vol. 22, No. 3-4, December 2006, pp. 181-195. Also see www.llnl.gov/casc/samrai.

[24]Brès, G. A., Brentner, K. S., Perez, G., and Jones, H. E., "Maneuvering rotorcraft noise prediction," *Journal of Sound and Vibration,* 275(3-5):719-738, August 2004.

[25]Farassat, F. and Succi, G. P., "The Prediction of Helicopter Discrete Frequency Noise," *Vertica,* 1983; 7(4):309-320.

[26]Ffowcs Williams, J. E. and Hawkings, D. L., "Sound Generated by Turbulence and Surfaces in Arbitrary Motion," *Philos. Trans. R. Soc. A,* 1962; 264(1151): 321-42.